Supporting Information

X-ray compatible microfluidics for in situ studies of chemical state, transport and reaction of light elements in an aqueous environment using synchrotron radiation.

Jason Brenker[a], Katja Henzler[b], Camelia N. Borca[b], Thomas Huthwelker[b]* and Tuncay Alan[a]*

a.Department of Mechanical and Aerospace Engineering, Monash University, Clayton, Australia.
b.Paul Scherrer Institute, Swiss Light Source, Villigen, Switzerland
*E-mail: thomas.huthwelker@psi.ch, tuncay.alan@monash.edu

S.1. Device Comparison
A detailed comparison of previous devices is presented in the main text, in the table below is a summary of the comparisons made to previous devices. The device presented by Nagasaka et al. and Huyke et al. offer comparable minimum time points, however due to the larger beam size neither can offer the spatial resolution presented in this work. Furthermore, the minimum temporal resolution quoted from Huyke et al. is in the direction of flow only, so the lateral diffusion cannot be mapped.

Table S1 Comaprison to existing devices

Ref	Chemical System	Window/Channel Material	Energy (keV)	Spot Size	Minimum t / Δt	Comments
Chan et al. 2007[51]	CdSe-to-Ag2Se nanocrystal cation exchange	1 µm SiN + 1 µm SU8 window Si channels	12.64-13	16 µm × 7 µm	8 ms / 4 ms	XAS Se K-edge in Fluo.
Oyanagi et al. 2011[39]	Synthesis of CdSe NP	Kapton capillary	12.64-13	1 mm x 0.5 mm	1 sec	XAS at Se K-edge in Fluo.
Best et al. 2016[49]	Photorereduction of FeIII species	Kapton window	7.10 – 7.30	~ 1mm	Pulse flow	XAS at Fe K-edge in Fluo.
Nagasaka et al. 2019[12]	Pyridine with water	100 nm SiN window PDMS channels	0.32 – 0.58	30 µm × 30 µm	3.2 ms / 7.1 ms	XAS at N-K edge in Fluo.
Chaussavoine et al. 2020[25]	Fe oxide NP formation	8 µm kapton window + 30 µm PDMS layer, PDMS channels	7.108 – 7.122	3.5 µm × 3.5µm	Several seconds	XAS at Fe K-edge in Fluo.
Huyke et al. 2021[50]	Ferricyanide with ascorbic acid	Fused silica channels, polyimide capillary 27 µm thick	7.108 – 7.122	510 µm	2.1 ms / 0.3 ms	XAS at Fe K-edge in Fluo.
Probst et al. 2021[38]	$CaCO_3$ precipitation	450 nm SiN PDMS channels	3.09 – 4.20	50 µm × 75 µm	10 ms / 1.8 ms	XAS at Ca K-edge in Fluo.
This work	$CaCl_2$ with Na_4EDTA	100 nm SiN window PDMS channel PDMS thin walls/Si	1.84 - 4.09	3 µm × 3 µm	2.25 ms / 0.365 ms	XAS at Ca K-edge in Fluo.

S.2. Fabrication

The fabrication procedure for both cast and drip molded PDMS channels and PDMS slab and silicon backed (SB) devices are shown below. To assist with alignment the 6-axis alignment stage depicted in Fig. S2 was utilized to align components quickly and precisely during the plasma bonding step.
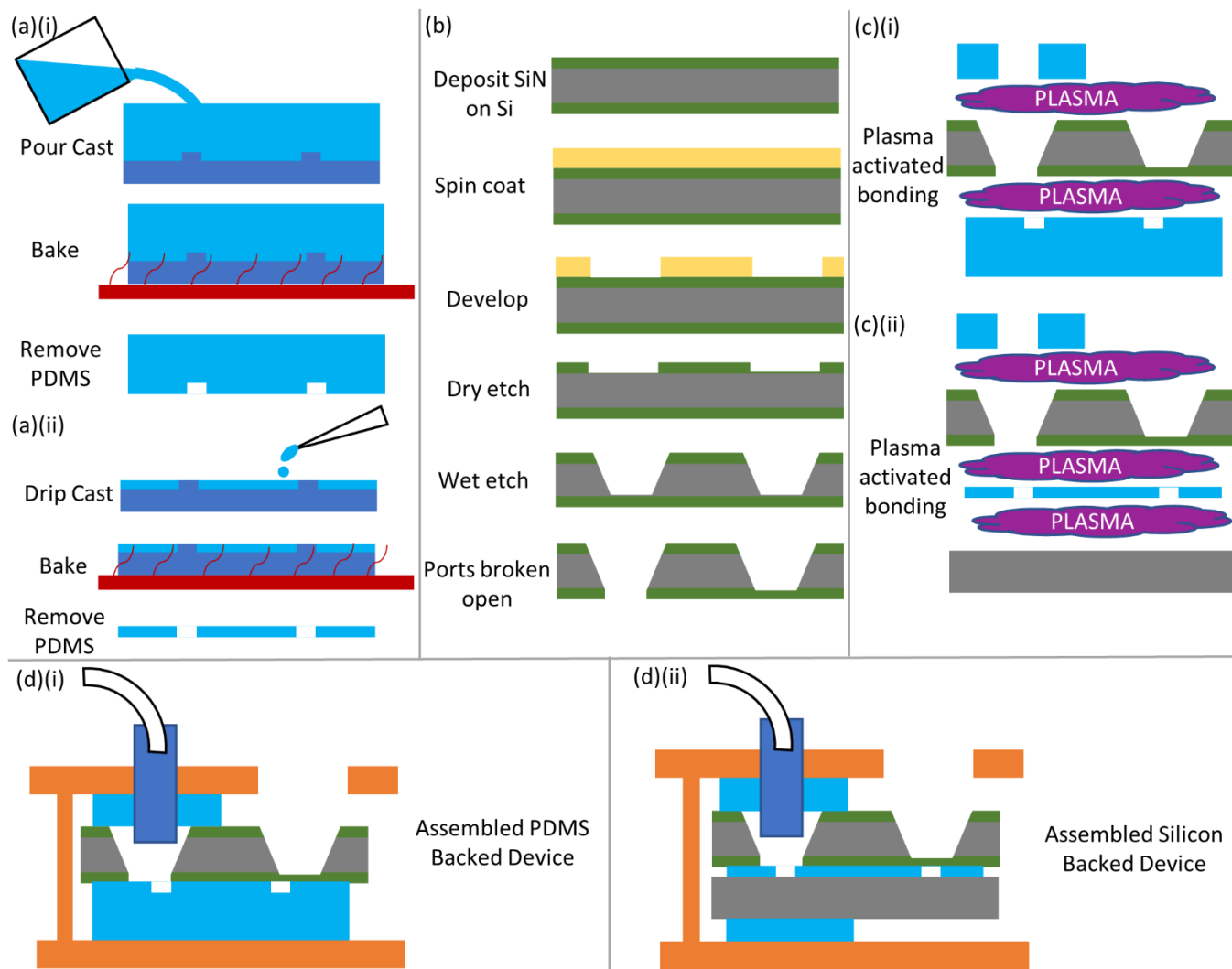

Fig. S1 ((a) Flow diagram of the key steps in the casting process for standard PDMS channels and thin films (drip casting). (b) Fabrication process of the SiN$_x$ membranes, beginning with SiN$_x$ deposited on Si wafers and spin coating of photoresist. The membrane locations are then patterned and etched as described before sacrificial membranes over the port regions are broken. (c) Plasma bonding of SiN$_x$ membranes, PDMS layers and Si to form microfluidic cells. (d) 3D printed housing and fluid connections are added to complete devices. The device assembly procedures are summarized in Supplementary Video 2.
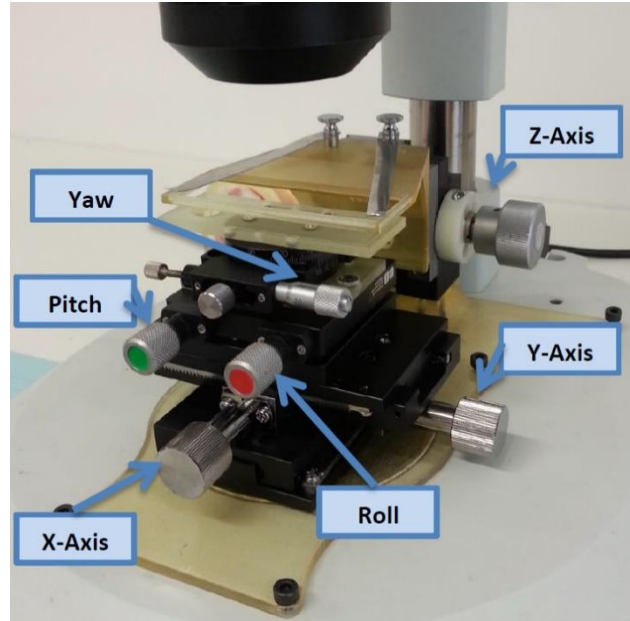
Fig. S2: 6-axis alignment stage fitted to stero microsope for precisce alignment durning plasma bonding.

S.3. Beam Damage

The below results are representative of the observed damage in PDMS channels with a $3\mu m^2$ focused beam. The images in c, and f, are of a SB device.
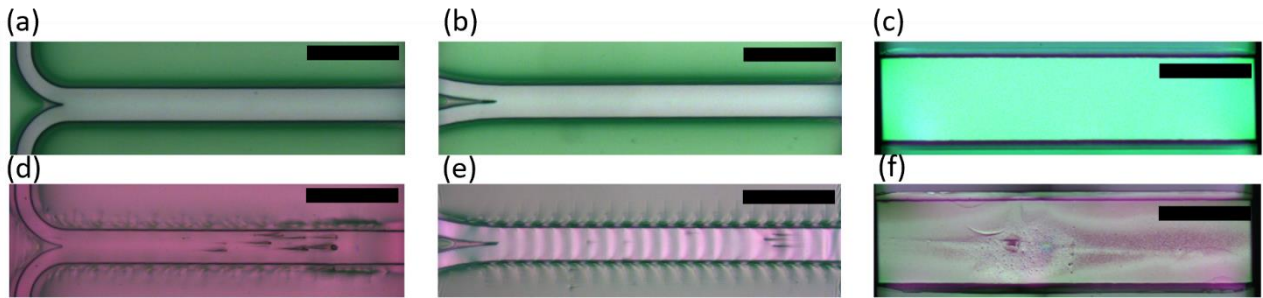

Fig. S3: Examples of observed beam damage for devices used in this study. a, b, and c represent depict channels before exposure and d, e, and f depict channels after exposure. A 3 μm² spot with a beam energy of 4050 eV produced these effects following scans of around 15 mins in duration over an 8 hour period. All scale bars 500 μm

S.4. Calculation of diffusion coefficient

S.4.1 Derivation of 1D Diffusion Equation:

Mathematically, the system comprises a coupled system with advective flow and diffusion, which cannot be solved with simple analytical equations.

The coordinate system used to model the microfluidic devices in this paper is visualized in Fig. S1. The liquid flows into the z direction, the y direction is normal to the window, and the x direction is across the width of the channel. Ignoring chemical reactions, the diffusion of a species in a laminar flow system requires solving the 3-dimensional diffusion equation for the steady state case

$$\frac{\partial n(x,y,z)}{\partial t} = D\left(\frac{\partial^2}{\partial x^2}n(x,y,z) + \frac{\partial^2}{\partial y^2}n(x,y,z) + \frac{\partial^2}{\partial z^2}n(x,y,z)\right) + v_z(x,y)\frac{\partial}{\partial z}n(x,y,z) \qquad (s1)$$

Where *D* is the diffusion constant, and *v(x,y)* is the velocity profile in the channel. While this equation

is not analytically solvable for the general case, certain approximations can be made. First, the main diffusive gradient is in x direction, while negligible in z (flow) direction. Hence, the $\frac{\partial}{\partial_z}$ terms can be ignored. [1]

The effect of the assumed velocity profile will be discussed further below, but here we consider its effect on diffusion in the vertical, y direction. Considering the simplest flow profile, where wall effects are neglected and there is a uniform velocity throughout the field, there would be no velocity gradient and no initial concentration gradient in the y direction.

Considering this case, dispersion could occur in the y direction in this system due to convection driven by a gradient in the velocity profile. This is commonly known as Taylor-Aris diffusion, which was first treated theoretically by Taylor[2] for circular pipes and later extended to rectangular ducts by Aris[3]. More recent work by Rahman et al. has found this effect can be ignored in rectangular ducts at sufficiently low values of Peclet numbers, Pe.[4]
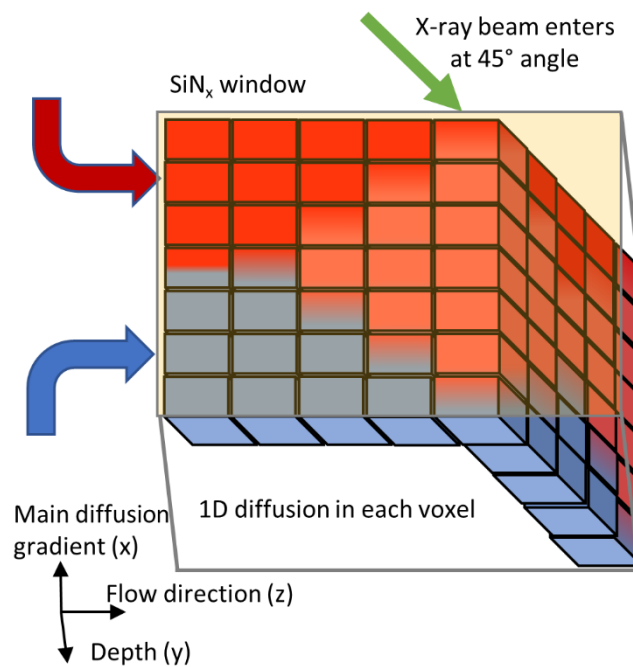

Fig. S4: Coordinate system and approximations to solve diffusion equation. Liquid flow is directed in z direction. The window is marked as orange rectangle. Red and blue color symbolizes the concentration of the two diffusing species. For plug-flow there is no flow profile and the solution in the different slabs move independent of each other. For non-plug flow conditions the travel time inside of the channel (fast speed) is fast compared to the one close to the window, implying more diffusion near the walls.

$$Pe = \frac{Lv}{D} \hspace{5cm} \text{(s2)}$$

L is the critical length, in our system the hydraulic diameter, v is the velocity at the centerline of the channel and D is the molecular diffusion coefficient. For our 200 µm by 90 µm channel the hydraulic diameter is 124 µm, the maximum velocity studied, obtained from equation 2, is 2.91×10^{-3} m.s^{-1}, and the smallest molecular diffusion coefficient considered for the online experiments was EDTA in table 1. This leads to a maximum Pe of 330, which is below the threshold of 1000 where 1D diffusion is considered dominant.[4] Thus the term $\frac{\partial^2}{\partial y^2} n(x, y, z)$ can also be neglected.

With the above assumptions equation s1 is reduced to Fick's second law

$$\frac{\partial c}{\partial t} = D \frac{\partial^2 c}{\partial x^2}$$
(s3)

Assuming diffusion into an infinite reservoir, and a stepwise initial concentration with a magnitude of c_0 at the channel center (x=0) equation s3 takes the form:

$$I(x,t) = \frac{c_0}{2} \cdot erfc\left(\frac{x - x_0}{d(t)}\right) + B$$
(s4)

Here *x* is the location from the centre of the channel, x_o. c_o represents the concentration at the inlet, represented by the fluorescence intensity, and B is the background signal. The background *B* can account for homogeneous contaminations in the system or other backgrounds, for example form elastic scattering. The term *d(t)* for each point is given by Equation s5.

$$d(t) = \sqrt{4 \cdot D \cdot t}$$
(s5)

Here, *D* is the diffusion coefficient of the ion of interest, and *t* is the travel time of the liquid after passing the Y-junction which at the entry of the chip.

The time *t* was calculated from the positions and velocities of the theoretical velocity distribution. Here we use the analytical model presented in Fig. 2e to find the diffusion time at each point in a cross section of the channel. Reformulating equation s5, one can find the relation *d(t)² = 4D(t-t0),* where t_0 is the start of the mixing time. This shows that d(t)² depends linearly on the diffusion constant, and *D* can be determined directly from the slope, even if the start of the diffusion is not exactly known, as shown in Fig. 3e.

As a single measurement is made for each x-z coordinate of the channel the analytical diffusion times are found through integration over the path of the beam in the fluid. Here we are faced again with our choice of velocity profile. With a plug flow assumption t is linearly related to distance from the inlet, z. Previous studies have argued that if the local velocity is within 95% of the maximum velocity the profile could be ignored.[5] However, in our system this threshold is met for only the middle 33% of the channel, thus any measurements outside this zone require consideration of the side wall effects. A solution would have been to increase the width of the channel but as discussed further in section 4.2.5, for membrane stability this was not achievable.

S.4.2 Beam Decay

An additional complicating factor unique to the measurement system presented here is the decay of x-ray intensity within the fluid. Unlike in previous studies working with optical measurement techniques the assumption of uniform sampling over the channel depth is not valid.[5] The decay of x-ray energy in a medium is described by the Beer-Lambert law, equation s6.

$$I(p) = I_0 e^{-\alpha p}$$
(s6)

I(p) is the intensity at some distance, *p*, into an attenuating substance, in this case water, I_0 is the initial intensity, α is the linear attenuation coefficient, and *p* is the path length into the substance. Given the x-rays must penetrate first to some depth into the fluid at an angle of 45° and then back out again at 45° the total path length is $2\sqrt{2}y$, where *y* is the vertical depth from the window. A channel depth of 90 μm and 45° incident angle, as used in this study, leads to a maximum geometric path length through the fluid of 255 μm.

To account for this decay each point measured in the x-z plane was treated as the integral of each voxel in the beams path, with this weighting applied as a function of depth. We have also assumed the diffusion time at a point in the fluid, t_{xyz}, is simply the local velocity divided by the distance from the inlet. The limits of integration in equation s7 are taken from the beam spot size, 3 μm in the x plane and a plane 45° from the z plane, and the beam path from the top to the bottom of the 90 μm channel, y direction.

$$t_{xz} = \int_{x-1.5}^{x+1.5} \left[\int_0^{90} \left[\int_{z+y-\frac{3\sqrt{2}y}{2}}^{z+y+\frac{3\sqrt{2}y}{2}} \left(\frac{z}{v(x,y)} \times e^{-\alpha_{in}\cdot\sqrt{2}y} \times e^{-\alpha_{out}\cdot\sqrt{2}y} \right) \partial z \right] \partial y \right] \partial x \qquad (s7)$$
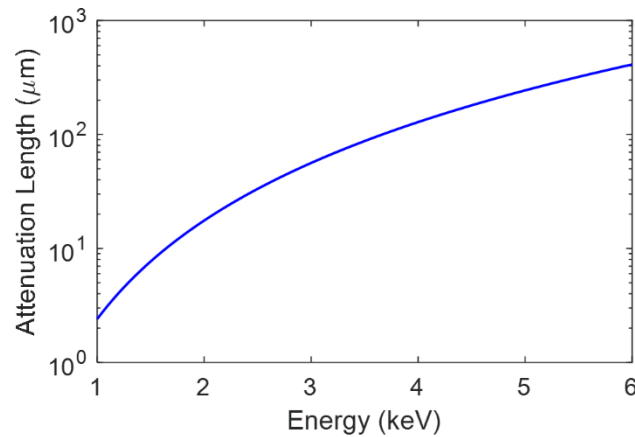

Fig. S5: Attenuation length of x-rays for the same in water for the energy range shown in (a). Attenuation length is defined as depth at which I/I0 has fallen to 1/e or approximately 13%.

As others have discussed the effects of beam angle on time resolution and the deviation of the velocity profile in a 403 μm channel, however they stated the velocity distribution has a SD of 10% due to the but that diffusion offsets this leading to deviation of less than 5%. They do not consider the beams decay and thus oversampling of low velocity regions at the top of the channel due to the higher energy range scanned, from 12.5 to 12.86 keV, where the penetration depth is around 3.8 mm.[6]
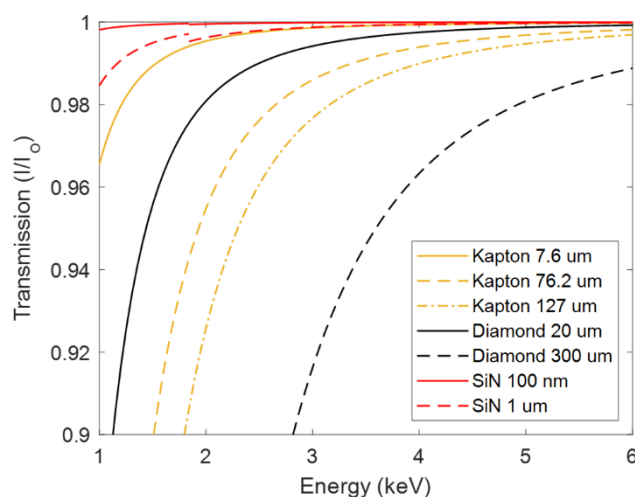

Fig. S6: Transmission for three x-ray window materials in common thicknesses for typical XAS energy range. Note only transmissions greater than 90% are shown.

The time resolution of any point is a function of the gradient in the flow velocity (see Fig. 2d), the area sampled considering the path of the beam, and the location in the channel measured. In Fig. S7 we show the combined effect of the Poiseuille flow and beam decay in our device as well as three similar studies from the literature. Fig. S7 indicates the average velocity of the channel depth probed as compared to the average velocity over the full channel depth. Clearly, a lower average velocity in the measured region results in later time points in a reaction being measured than if this effect were not considered, and a broader time resolution between points.
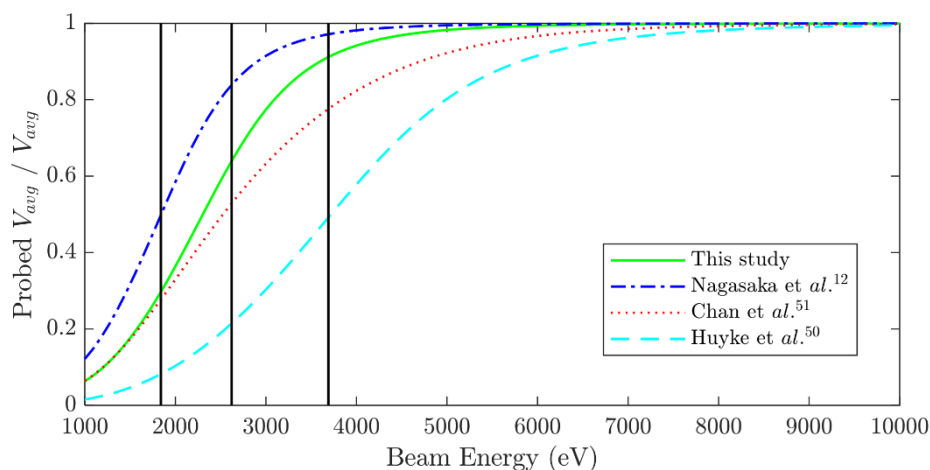

Fig. S7: Change in average velocity of sampled region considering combined effect of Poiseuille flow profile and beam decay. The three vertical black lines represent the energy of the three key white lines used in this study, Si Kα (1840 eV), Ca Kα (3690 eV), and Cl Kα (2622 eV). Probed V_{avg} is the average velocity in the region of the channel probed

To compare the earliest measurable time points and time resolution in different channel geometries we compare 6 channels with different aspect ratios (width/depth) but the same cross-sectional area, volumetric flowrate, and beam spot size. Therefore, any differences in time points or temporal resolution are due to changes in the flow profile and beam penetration depth.
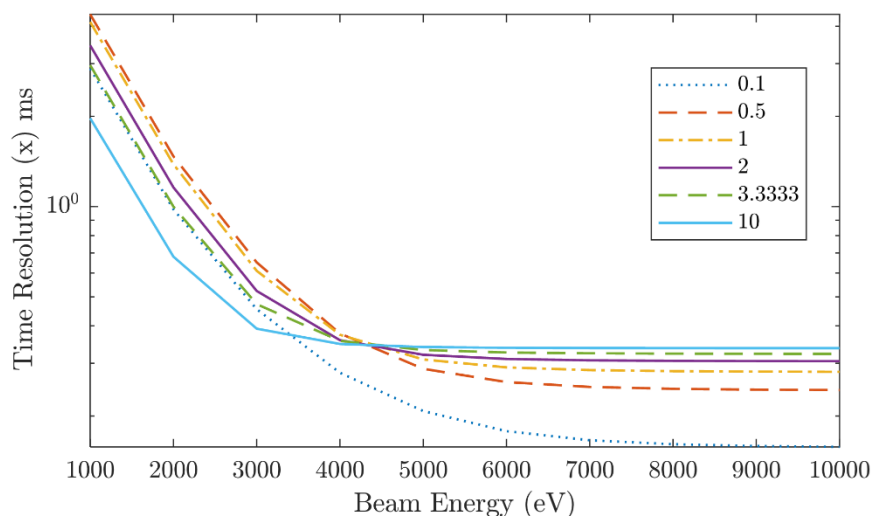

Fig. S8: Combined effect of Poiseuille flow and beam decay on time resolution for a channel with a cross-sectional area of 1.8×10^4 μm^2, and flow rate of 17.2 $\mu l.min^{-1}$. At energies below 5 keV different aspect ratios exaggerate the effect of the flow profile on

Above 5 keV as expected a deeper channel (aspect ratio 0.1) results in a higher time resolution as more of the higher velocity flow in the center of the channel is measured before the beam decays. However, at lower x-ray energies the shallower channel (aspect ratio 10) results in a smaller time resolution as higher velocity flow at the channel center is still probed by the beam as compared to the deeper channel where the x-ray energy is absorbed within the boundary region near the wall.

Fig. S9 shows that each aspect ratio channel has a threshold above which the minimum accessible time for is not sensitive to x-ray energy. The trend in this figure can be understood by considering Fig. 2e, as the x-ray energy is reduced less of the channel depth is probed by the beam. First the slower flow at the bottom of the channel is neglected, thus increasing the average velocity of the probed region, and reducing the time point. However, once the probed region begins to neglect flow from the center of the channel at low x-ray energies (below 2 keV) the average velocity of the probed region begins to decrease, thus increasing the time points again.
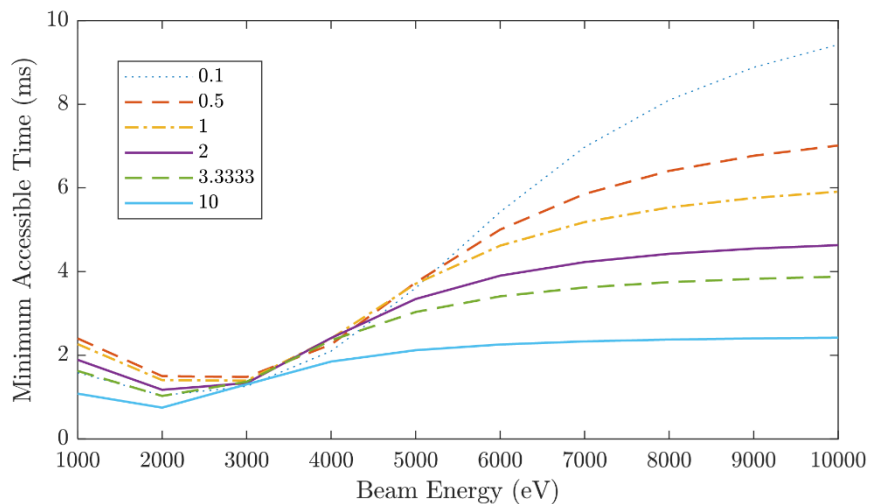

Fig. S9: Combined effect of Poiseuille flow and beam decay on minimum accessible time points for a channel with a cross-sectional area of 1.8×10^4 μm^2, and flow rate of 17.2 $\mu l.min^{-1}$. At energies below 5 keV different aspect ratios exaggerate the effect of the flow profile on the velocity of the sampled region, and so the time points.

S.5 Droplet-Based Data Analysis

As only the count rates for when droplets were passing the beam were desired an indicator ion was needed, as the Ca signal was not distinguishable above the noise for beam energies below its k-edge of around 4038 eV. If the droplet production rate had been synchronised with the SDD this would not be necessary. Cl was used as an indicator as it has a lower energy k-edge of around 2822 eV.

To convert this data from raw photon counts to a spectrum, a number of data processing steps were used. First the detector measures the energy and reports their arrival time of photons with an intrinsic time of 20 ns. The data was then binned into time intervals of 2 ms and the histogram of counts per time bin were found. The area under these histogram curves indicated the count rate per time bin, per energy level, which was divided by the bin width to give the counts per second as shown in Fig. 7 (c-d).

A threshold was set on the Cl count rate, and only time bins where this was exceeded were then averaged over each measurement cycle of 3 seconds per input energy level. Finally, the count rate per input energy was combined over the entire energy range tested to produce the plot in Fig. 8 (b),

showing the expected Ca K-edge for this energy range. This is plotted against a spectrum measured for a similar microfluidic device operated in a flow through mode, that is filled entirely with $CaCl_2$, allowing a spectrum was measured over a much longer time period of 25 minutes with steps in energy levels providing better resolution.

In this experiment the counts per second (cps) for Ca at a concentration of 100 mM as part of a $CaCl_2$ solution was found to be around 30,000 cps at the while line (maximum value at the K-edge).

For the spectrum presented in Fig. 7b a 3 second scan per energy level was employed. Coupled with a switching time between energy levels of 20 seconds, this resulted in a total measurement time of approximately 7 minutes to produce the spectrum shown. This methodology can be further extended by combining droplets on-chip and collecting spectra at multiple spatial locations along the serpentine channel, effectively providing different time points in the reaction being studied. Whilst a promising demonstration of in situ droplet-based measurements, there were a number of key challenges in operating this device.

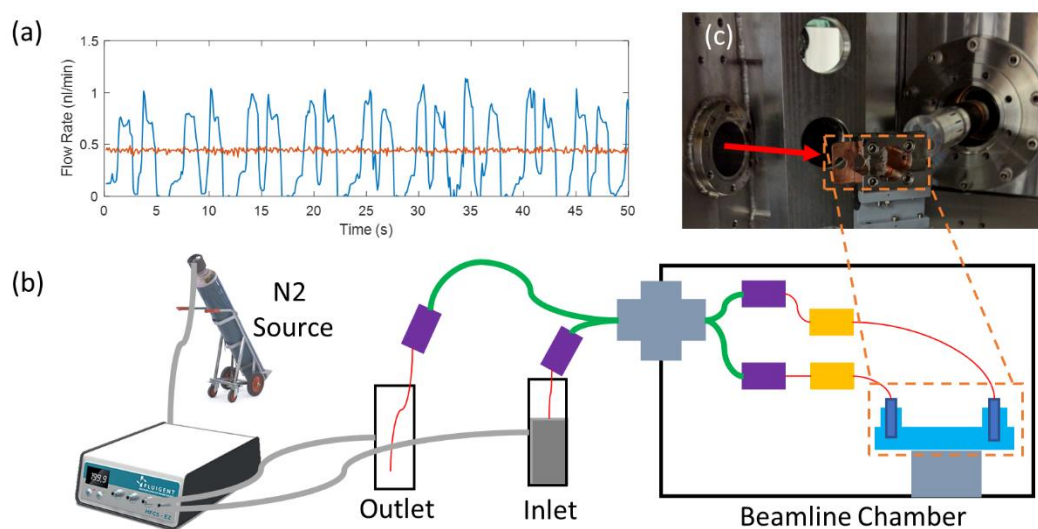### S.6 Fluid Connections and Pumping

Figure S10 (a) Measured flowrate for two inlet lines, with spikes in the blue plot indicating droplet generation events while the orange plot indicates a inlet line forming a continuous laminar flow without forming droplets (b) Schematic layout of the connections to the microfluidic device in the vacuum chamber, including pressure pump, and fluid resevoirs. The 1/4 inch OD PTFE tubing shown in green was 1.4 m long running through the stainless steel flange shown in grey. This larger tubing was connected with ferrules, shown in purple, to the microbore tubing in which the sample was pumped, shown in red. This innner tubing had a total length of 1.7 m per inlet line. (c) Photograph illustrating position of incoming beam, shown as a red arrow, relative to the the device. The silicon drift detector is behind the mount at a 45º to the incoming beam.

S.7 Details of the numerical model

Key parameters. Through the use of COMSOL Multiphysics the reaction of Ca bound to Calmagite (PR) with EDTA was modeled.

$$Ca\text{-}PR^{2+} + EDTA^{4-} \rightarrow PR + [CaEDTA]^{2-} \tag{5}$$

The parameters used to setup the model are presented in Table S2.

Diffusion constants were found with the Stokes-Einstein equation

$$D = \frac{kT}{b\pi\mu r} \tag{6}$$

where, k is the Boltzmann constant, T is the temperature, b is a constant dependent on the size of the diffusing

Table S2. Key parameters used in numerical model of diffusion

	Molecular Diffusion Coefficient	Molecular Diameter [Å]
CaCalmagite	9.910×10^{-10}	8.585
EDTA	1.094×10^{-9}	7.776
Calmagite	1.036×10^{-9}	8.212
CaEDTA	1.105×10^{-9}	7.702
Cl	2.011×10^{-9}	4.231
$CaCl_2$	7.08×10^{-10}	Experimentally determined
Density [kg.m^{-3}]	999.6	
Dynamic Viscosity [Pa.s]	1.009	

molecules relative to the medium, in our case taken to be 6, µ is the dynamic viscosity of the liquid medium, and r is the diffusion molecule radius.

The molecular radius was found for each of the components of the reaction with the molecular modeling suite VEGA ZZ. Three-dimensional structures of Calmagite and EDTA were downloaded from the PubChem database [7, 8]. The diameter of each was then measured before and after modifying both structures to incorporate a bound Ca ion, these diameters and calculated diffusion constants are provided in Table 1. The numerical model of diffusion and reaction within a microfluidic channel was developed in COMSOL Multiphysics v5.1.

In this study we present a three-dimensional model to capture the behaviour of the system. The fluid and molecular properties defined in table 1 and the geometry used to create the original moulds were applied to a fluid domain which utilized the Navier-Stokes equations. The mass transport properties were defined through convection and diffusion, and within the 'reacting flow in porous media' module (no porous elements were included in this model) the reactions which consumed CaCalmagite and EDTA and produced Calmagite and CaEDTA were defined. The reaction rate taken from the literature which indicates at 20° the reaction constant of the formation of CaEDTA is $5.4 \times 10^9 s^{-1}M^{-1}$ [9].

Supplementary References:

1.   Kamholz, A. E.; Yager, P., Molecular diffusive scaling laws in pressure-driven microfluidic channels: deviation from one-dimensional Einstein approximations. *Sensors and Actuators B: Chemical* **2002,** *82* (1), 117-121.
2.   Taylor, G. I., Dispersion of soluble matter in solvent flowing slowly through a tube. *Proceedings of the Royal Society of London. Series A. Mathematical and Physical Sciences* **1953,** *219* (1137), 186-203.
3.   Aris, R., On the dispersion of a solute by diffusion, convection and exchange between phases. *Proceedings of the Royal Society of London. Series A. Mathematical and Physical Sciences* **1959,** *252* (1271), 538-550.
4.   Rahman, M. M.; Moinuddin, K. A.; Thorpe, G. In *A numerical study of dispersion in laminar flow in non-circular ducts*, Proceedings of the 19th Australasian Fluid Mechanics Conference, AFMC 2014, Australasian Fluid Mechanics Society (AFMS): 2014.
5.   Kamholz, A. E.; Weigl, B. H.; Finlayson, B. A.; Yager, P., Quantitative analysis of molecular interaction in a microfluidic channel: the T-sensor. *Analytical chemistry* **1999,** *71* (23), 5340-5347.
6.   Chan, E. M.; Marcus, M. A.; Fakra, S.; ElNaggar, M.; Mathies, R. A.; Alivisatos, A. P., Millisecond kinetics of nanocrystal cation exchange using microfluidic X-ray absorption spectroscopy. *The Journal of Physical Chemistry A* **2007,** *111* (49), 12210-12215.
7.   Information, N. C. f. B., EDTA disodium salt, CID=13020083. *PubChem Database* **2020**.
8.   Information, N. C. f. B., Calmagite, CID=2530. **2020**.
9.   Bryson, A.; Fletcher, I., Ligand exchange kinetics in the calcium-EDTA system. *Australian Journal of Chemistry* **1970,** *23* (6), 1095-1110.